Biosensors and Bioelectronics 129 (2019) 42–49

Contents lists available at ScienceDirect

Biosensors and Bioelectronics

journal homepage: www.elsevier.com/locate/bios

Multifunctionalized ZIFs nanoprobe-initiated tandem reaction for signal amplified electrochemical immunoassay of carbohydrate antigen 24-2

Yun Zheng, Zhanfang Ma*

Department of Chemistry, Capital Normal University, Beijing 100048, China

ARTICLE INFO

Keywords:
Amperometric immunosensor
Zeolitic imidazolate framework
Tandem reaction
Sandwich-type
Tumor marker

ABSTRACT

Based on multifunctionalized zeolitic imidazolate frameworks (ZIFs)-initiated cascade reaction triggered signal amplification strategy, a novel sandwich-type amperometric immunosensor was constructed for ultrasensitive detection of carbohydrate antigen 24-2 (CA 242). The methylene blue-glucose oxidase-ZIF-8/reduced graphene oxide-Au (MB-GOx-ZIF-8/Au-rGO) was synthesized by a facile coprecipitation method for enzyme immobilization and redox species loading. The multifunctionalized ZIFs conjugated with labeling antibodies were employed as immunoprobe. In the presence of glucose, tandem reaction was driven by the immunoprobe to catalyze the glucose oxidation to yield H_2O_2. Simultaneously, the generated H_2O_2 induced the decomposition of poly(anilineboronicacid) (PABA)/poly(vinyl alcohol) (PVA) films on substrate, which made the PVA chains breaking away from PABA polymer. Due to the poor conductivity of PVA chains, this decomposition reaction can amplify the current signal. The current difference (ΔI) caused by per unit concentration target with tandem reaction amplification was elevated prominently, resulting in ultrasensitive analytical performance of the immunosensor. Under optimal conditions, the proposed immunosensor displayed wide linear range from 0.001 to 1000 U mL^{-1} with an ultralow limit of detection 69.34 μU mL^{-1} (S/N = 3). This method successfully implemented functionalized ZIFs in immunoprobe construction for sensitivity amplification, providing a promising strategy to construct ultrasensitive immunosensing platform for analysis of other tumor marker.

1. Introduction

Design and development of ultrasensitive analytical assays for tumor markers are imperative for prevention, non-invasive diagnosis and treatment of cancer (Lin and Ju, 2005; Zhuo et al., 2014). According to reports, carbohydrate antigen 24-2 (CA 242) was one of significant potential diagnostic serum tumor markers complementing CA 199 in early pancreatic cancer and valuable complementary biomarker to carcinoembryonic antigen (CEA) in prognosis prediction and treatment of colorectal cancer (Chen et al., 2015; Furuya et al., 1996; Hasmik et al., 2011). Several analytical methods have been developed for sensitive detection of CA 242, including magnetic resonance imaging (Iishi et al., 1986), ultrasonographic examination (Villeirs et al., 2010) and fluorescent assay (Pujol et al., 1993). Compared to these methods, amperometric immunosensors have gained greater attention owing to the advantages of rapid detection, small volumes of sample and sensitive detection performance (Kaushik et al., 2013; Li et al., 2017, 2015). For sandwich amperometric immunsensors, the improvement of sensitivity depends on elevating the signal difference (ΔI) caused by per unit concentration analyte (Tang et al., 2016; Zheng and Ma, 2018). Application of effective sensitivity enhancement strategies to sandwich immunosensor for reaching ultralow limit of detection is critical to satisfy the demand of modern clinical prevention and diagnosis (Tang and Ma, 2017; Zhou et al., 2017).

Signal amplification based on facile design of functional nanoprobes is an effective approach to improve the performance of sandwich electrochemical immunosensor (Yang et al., 2018; Zhang et al., 2017). Unique chemical and physical properties make functional nanomaterials at nanoscale prominent carrier materials to combine with enzyme and redox species for assembling high performance electrochemical nanoprobes (Peng et al., 2014; Hu et al., 2018; Wang and Ma, 2018). Enzyme-functionalized nanoprobes have been successfully developed by employing nanomaterials, such as gold nanoparticles, carbon tubes and mesoporous silica nanoparticles, as nanocarrier to load different enzyme molecules as immunoprobe (Lai et al., 2017; Liu et al., 2016; Malhotra et al., 2010; Su et al., 2017). At present, a variety of sensitive sandwich electrochemical immunoassays have been constructed based on these nanoprobes. However, the preparations required complicated chemical modification to immobilize enzyme molecules under tightly controlled environmental conditions (Du et al., 2011; Zhao et al.,

* Corresponding author.
E-mail address: mazhanfang@cnu.edu.cn (Z. Ma).

https://doi.org/10.1016/j.bios.2019.01.016
Received 16 November 2018; Received in revised form 19 December 2018; Accepted 4 January 2019
Available online 15 January 2019
0956-5663/

2016). Therefore, it is of significant importance to design a functional nanoprobe, which can be prepared by facile and easily-achieved approach for signal loading and enzymes immobilization at the same time. Recently, porous materials have showed great potential in the field of nanoprobe construction due to their porosity and structural flexibility for molecules loading (Kreno et al., 2012; Li et al., 2018; Zhang et al., 2018). As an important kind of porous materials, zeolitic imidazolate frameworks (ZIFs) are rapidly emerging taking advantages of large specific surface area for high loading capacity and strong interactions towards enzymes to avoid the leakage of enzymes (Wang et al., 2017, 2018; Chen et al., 2014). Moreover, the great thermal and chemical stabilities and easy synthesis method make ZIFs an attractive support nanomaterial for signal molecules and enzymes loading under mild conditions (Hou et al., 2015; Shi et al., 2016). For example, Lyu et al. (2014) prepared protein-embedded ZIF-8 with enhanced biological activities by one-pot synthesis. However, the direct application of ZIFs in immunoprobe is limited by the weak electrocatalytic ability and poor conductivity. Introducing highly electrochemical materials such as reduced graphene oxide (rGO) into ZIFs and introducing signal amplification reaction into immunosensing platform will be two promising strategies to enhance the performance of functionalized ZIFs nanoprobes.

In this work, multifunctionalized ZIFs, methylene blue-glucose oxidase-ZIF-8/reduced graphene oxide-Au (MB-GOx-ZIF-8/Au-rGO) composite, was fabricated as nanoprobe. The nanoprobe initiated tandem reaction for signal amplification. This signal enhancement strategy was implemented into sandwich-type immunosensor for ultrasensitive detection of CA 242. The signal amplification strategy based on ZIFs nanoprobe-initiated tandem reaction showed the following advantages: (1) a facile nanoprobe construction method was developed to integrate redox species, enzyme and conductivity material with ZIFs under mild condition, which enabled the multifunctionalized ZIFs to have biocatalytic ability and high electrochemical current; (2) the glucose-triggered biocatalytic reaction and H_2O_2-induced films decomposition reaction were cascaded on the immunosensing interface, which realized the signal amplification while reducing the processing steps on the electrode surface; (3) The cascade reaction amplified the signal difference (ΔI) caused by per unit concentration target and improved the sensitivity of sandwich-type immunosensor consequently. The proposed analytical method showed prominent performance in human serum sample assay, indicating the promising potential application in clinical diagnosis.

2. Experimental

2.1. Materials and apparatus

CA 242 and CA 242 antibody were purchased from Shanghai LincBio Science Co., Ltd (Shanghai, China). The other details are provided in Supplementary material (Section S1).

2.2. Synthesis of the ZIF-8, MB-GOx-ZIF-8, Au-rGO, MB-GOx-ZIF-8/Au-rGO nanocomposites and labeling antibody (Ab_2)-MB-GOx-ZIF-8/Au-rGO

ZIF-8 was synthesized according to the previous literature (Pan et al., 2011). 4.00 mL, 0.31 M $Zn(NO_3)_2{\cdot}6H_2O$ aqueous solution was added dropwise into 40.00 mL, 1.25 M 2-methylimidazole aqueous solution with vigorous stirring at 25 °C for 30 min and the mixture became milky. Then, the precipitate was collected by centrifugation at 6000 rpm for 10 min and washed with water for three times. The precipitate was dried at 60 °C for 24 h under vacuum to obtain ZIF-8 powder. MB-GOx-ZIF-8 nanocomposites were preparation by one-pot synthesis of protein-embedded ZIFs method. 2.00 mL, 10 mg mL^{-1} MB aqueous solution was mixed with 4.00 mL, 0.31 M $Zn(NO_3)_2{\cdot}6H_2O$ aqueous solution and stirred for 5 min 2.00 mL, 10 mg mL^{-1} GOx solution was mixed with 2.00 mL, 3 mg mL^{-1} polyvinylpyrrolidone (PVP) solution to obtain the PVP-modified GOx. Then, the PVP-modified GOx aqueous solution and the mixture solution of MB and $Zn(NO_3)_2{\cdot}6H_2O$ were added into 40.00 mL, 1.25 M 2-methylimidazole aqueous solution respectively with stirring at 25 °C for 30 min. The product was obtained by centrifugation at 6000 rpm for 10 min and washed 3 times with water. The product was resuspended in 10.00 mL water. The preparation of Au-rGO was performed by the citrate-mediated reduction of GO and HAu_4Cl. 4.00 mL 1.00 mg mL^{-1} GO aqueous solution was added into 25.00 mL 0.05% HAu_4Cl aqueous solution with stirring for 2 h. 1.20 mL, 0.20 M sodium citrate aqueous solution was added into the mixture with stirring for 1 h. Then the mixture solution was heated reflux for 1 h. After centrifugation at 10,000 rpm, Au-rGO was washed with water for three times and redispersed in 8.00 mL deionized water. The concentration of GO was optimized shown in supplementary material. To obtain MB-GOx-ZIF-8/Au-rGO nanocomposites, 8.00 mL Au-rGO dispersion was mixed with 1.00 mL, 10.00 mg mL^{-1} MB and stirred for 10 min. Then, 2.00 mL MB-GOx-ZIF-8 dispersion was added into the mixture solution with stirring for 1 h. After centrifugation at 6000 rpm for 10 min and washing with water for three times, the product was retrieved as 8.00 mL dispersed solution. 100 μL, 1 mg mL^{-1} CA 242 antibody (Ab_2) was added into 2.00 mL dispersion of MB-GOx-ZIF-8/Au-rGO and stirred at 25 °C for 12 h. After that, 1.00 mL, 1.0 wt% BSA solution as blocking agent was added into the mixture and stirred for 1 h. Then, the Ab_2-MB-GOx-ZIF-8/Au-rGO labels were centrifuged and washed by 10 mM phosphate buffer (pH = 7.4), then dispersed in 2.00 mL, 10 mM phosphate buffer (pH = 7.4) and stored at 4 °C. The preparation method of Ab_2-MB/Au-rGO was shown in Supplementary material (Section S2).

2.3. Synthesis of PABA polymer and PABA/Au-rGO nancomposites

Poly(anilineboronicacid) (PABA) polymer was synthesized according to the previous literature (Li et al., 2011). 27 mg 3-aminophenylboronic acid monohydrate (APBA), 16 mg NaF, and 5 mg cetyltrimethylammonium bromide (CTAB) were dissolved in 5.00 mL, 0.1 M H_2SO_4 aqueous solution. After that, 5 mL, 0.02 M ammonium peroxydisulfate (APS) aqueous solution was rapidly added into the above mixture in one portion. The polymerization reaction was carried out under static conditions at 25 °C for 24 h. After centrifugation at 8000 rpm for 10 min, PABA was washed with water for five times and redispersed in 10.00 mL deionized water. 2.00 mL PABA dispersion was mixed with 2.00 mL Au-rGO dispersion and stirred for 30 min. After centrifugation at 8000 rpm and washing for water for three times, PABA/Au-rGO was obtained and redispersed in 4.00 mL water.

2.4. Construction of the immunosensing platform

Glassy carbon electrodes (GCE) were polished with 0.05 μm alumina powders for 10 min and ultrasonicated in ethanol and deionized water for 1 min respectively. 20 μL PABA/Au-rGO dispersion was dropped on the surface of GCE and dried in 37 °C dryer. 10 μL, 1 mg mL^{-1} poly (vinyl alcohol) (PVA) solution was dropped on the GCE for 30 min and combined with PABA by boronate ester bonds. PVA/PABA-Au-rGO/GCE was washed by deionized water to remove uncombined PVA chains. 50 μL, 200 μg mL^{-1} CA 242 antibody (Ab_1) was incubated on PVA/PABA-Au-rGO/GCE for 12 h at 4 °C. To block any non-specific binding sites, 1.0 wt% BSA solution as blocking agent was incubated on Ab_1/PVA/PABA-Au-rGO/GCE for 1 h at 37 °C. After each modification process, the modified electrodes were washed by deionized water.

2.5. Electrochemical measurement

20 μL, 1 U mL^{-1} CA 242 antigen standard solutions were incubated on the Ab_1/PVA/PABA-Au-rGO/GCE for 1 h. Then, CA242/Ab_1/PVA/PABA-Au-rGO/GCE was washed carefully to remove unbounded CA 242 antigen. 50 μL Ab_2-MB-GOx-ZIF-8/Au-rGO labels dispersion was

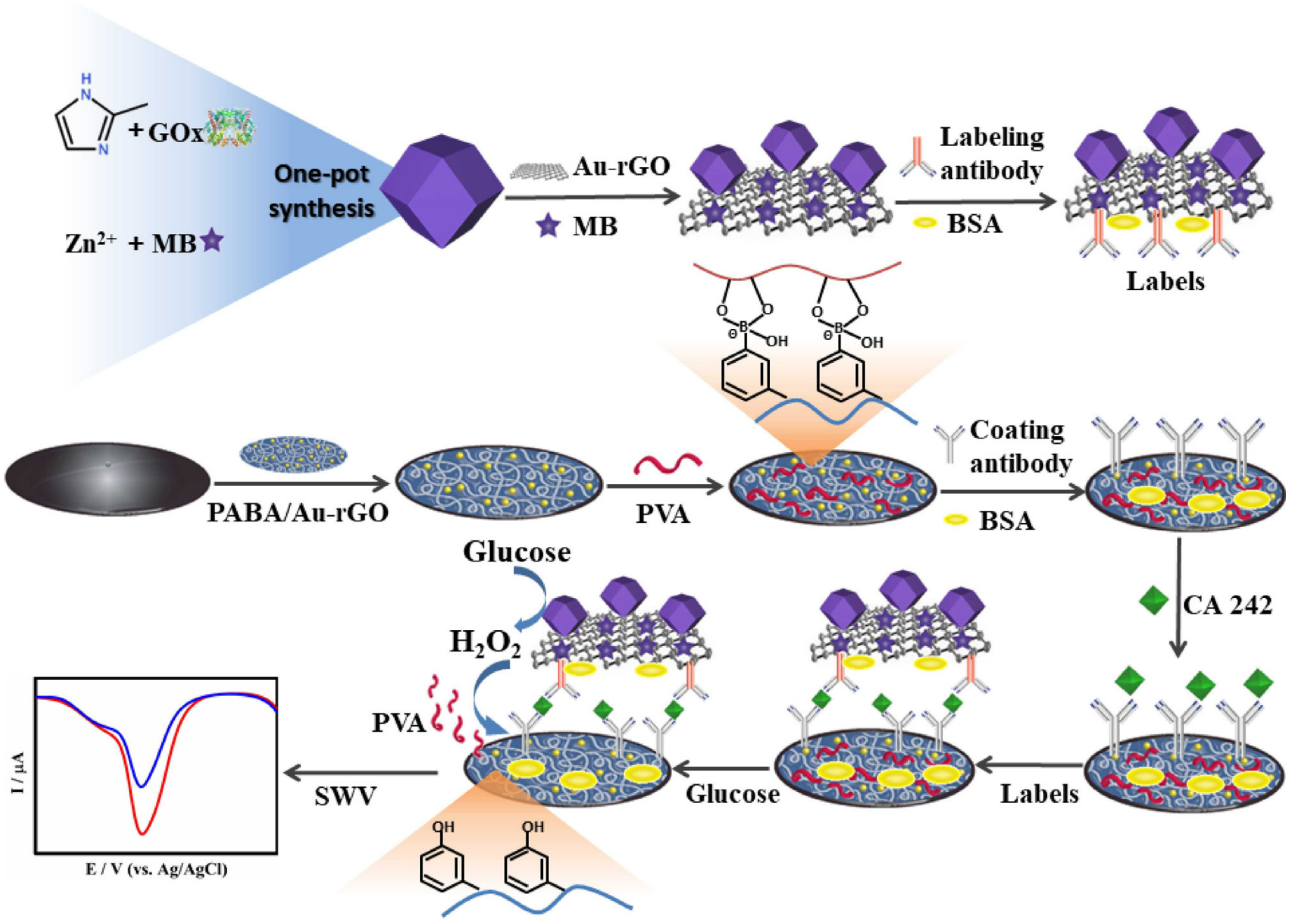

Scheme 1. Schematic illustrations of the multifunctionalized ZIFs nanoprobe-initiated tandem reaction for signal amplified electrochemical immunoassay.

dropped on CA 242/Ab_1/PVA/PABA-Au-rGO/GCE for 50 min at 37 °C. The modified electrodes were washed carefully to remove unbounded labels. 50 μL glucose solution was dropped on the surface of modified electrodes and PVA/PABA film decomposed almost completely in 30 min in the presence of 50 mM glucose at pH 7.4. The modified electrodes were washed with 10 mM phosphate buffer (pH = 7.4) to remove the decomposed PVA chains. Finally, the square wave voltammetry (SWV) measurement was conducted from −0.8 to 0.2 V in 10 mM phosphate buffered solution containing 0.1 M KCl (pH 7.4) with pulse amplitude of 25 mV and an increase potential of 4 mV.

3. Results and discussion

3.1. Principle of the proposed amperometric immunosensor

The stepwise construction procedure and detection principle of the proposed amperometric immunosensor were demonstrated in Scheme 1. Functionalized ZIF-8 nanocomposites were preparation by one-pot synthesis for redox species MB and GOx loading. Au-rGO nanosheets were combined with functionalized ZIF-8 and MB through electrostatic interaction to improve conductivity of nanocomposites and loading capacity of redox species MB. Labeling antibody (Ab_2) was conjugated with MB-GOx-ZIF-8/Au-rGO due to the interaction between antibody and gold nanoparticles. PABA/Au-rGO was designed as the substrate of immunosensor to enhance the conductivity of sensing interface. Because of the complexation effect between phenylboronic acid (PBA) groups provided by PABA polymer and 1,2- or 1,3- diols in PVA chains (Kuivila and Armour, 1957), PVA chains were immobilized on PABA polymer to form PABA/PVA self-assembled films. Au nanoparticles on the Au/rGO captured coating antibody (Ab_1). When the target CA 242 existed, Ab_2-MB-GOx-ZIF-8/Au-rGO nanoprobe was captured via antibody-antigen reaction. With the presence of glucose, the nanoprobe catalyzed the oxidation of glucose to produce gluconic acid and H_2O_2. Then, the H_2O_2 induced decomposition of PVA/PABA films at physiological pH and the unbounded PVA chains broke away from substrate (Sato et al., 2014, 2015). Due to the poor conductivity of PVA chains, this decomposition reaction amplified the current signal. A prominent current increase with SWV measurements elevated the current differences caused by per unit concentration target. Benefited from the multifunctionalized ZIFs nanoprobe-initiated tandem reaction, a novel sensitivity amplification strategy was developed for ultrasensitive detection of CA 242.

3.2. Characterization of functionalized ZIFs nanoprobe

Surface charges of MB-GOx-ZIF-8 and Au-rGO were evaluated using electrophoretic light scattering technique (Fig. S1). The zeta potential of MB-GOx-ZIF-8 was 17.8 mV (Fig. S1A) and the zeta potential of Au-rGO was −42.3 mV shown in Fig. S1B, indicating MB-GOx-ZIF-8 and Au-rGO were combined through electrostatic interaction. The morphologies of MB-GOx-ZIF-8, Au-rGO and MB-GOx-ZIF-8/Au-rGO were characterized by transmission electron microscope (TEM). MB-GOx-ZIF-8 particles displayed hexagonal morphology with diameter 300–500 nm shown in Fig. 1A. For Au-rGO, Au nanoparticles were densely distributed on rGO sheets as shown in Fig. 1B. After the combination of MB-GOx-ZIF-8 and Au-rGO, the isolated MB-GOx-ZIF-8 particles were anchored on Au-rGO sheets (Fig. 1C). The energy dispersive X-ray spectroscopy (EDS) patterns showed the chemical compositions of MB-GOx-ZIF-8, Au-rGO and MB-GOx-ZIF-8/Au-rGO. C, N, O and Zn elements were confirmed, which were derived from MB-GOx-

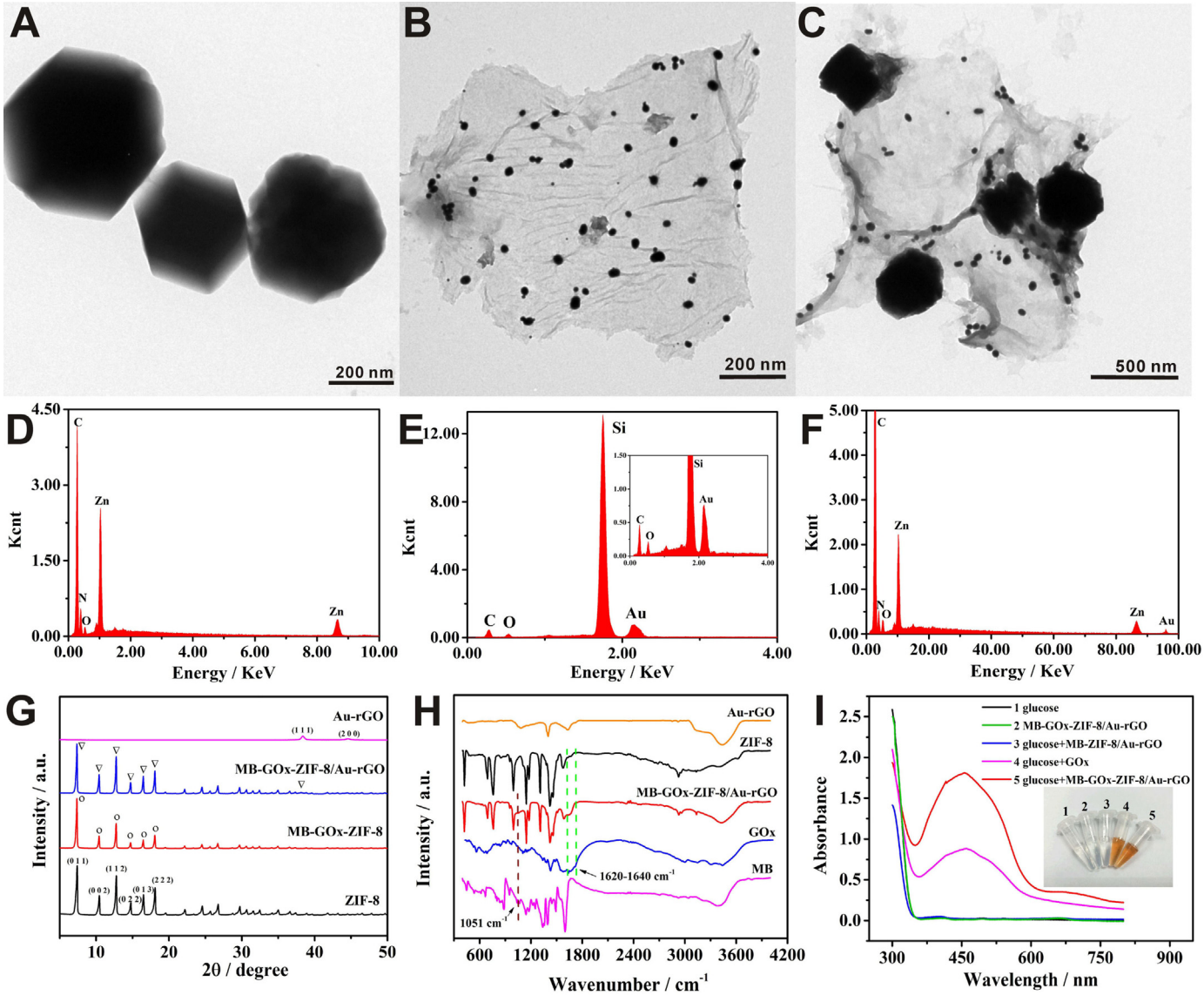

Fig. 1. Characterization of functionalized ZIFs nanoprobe. TEM images of MB-GOx-ZIF-8 (A), Au-rGO (B), and MB-GOx-ZIF-8/Au-rGO (C). EDS of MB-GOx-ZIF-8 (D), Au-rGO (inset: magnified one) (E), and MB-GOx-ZIF-8/Au-rGO (F). XRD patterns of ZIF-8, MB-GOx-ZIF-8, MB-GOx-ZIF-8/Au-rGO, and Au-rGO (G). FTIR spectra of MB, GOx, ZIF-8, and MB-GOx-ZIF-8/Au-rGO (H). UV/Vis absorbance spectra and visual color changes of five different samples from o-dianisidine indicator system colorimetric assay (I).

ZIF-8 particles (Fig. 1D). As shown in Fig. 1E, C, O and Au elements consisted in Au-rGO nanosheets. Since Au-rGO nanosheets were measured on the silicon wafer, Si element was derived from silicon wafer. Compared with MB-GOx-ZIF-8, MB-GOx-ZIF-8/Au-rGO composites contained Au element, which derived from Au nanoparticles on rGO nanosheets, indicating the successful combination of MB-GOx-ZIF-8 and Au-rGO (Fig. 1F). The powder X-ray diffraction (XRD) spectra of ZIF-8, MB-GOx-ZIF-8, MB-GOx-ZIF-8/Au-rGO and Au-rGO were shown in Fig. 1G. The characteristic diffraction peaks of Au nanoparticles on Au-rGO were found at 38.10° and 44.31° corresponds to the (1 1 1) and (2 0 0) plane which is consistent with the JCPDS ref. No 89–3697. ZIF-8 exhibited the characteristic peaks at 7.39°, 10.44°, 12.78°, 14.76°, 16.49° and 18.10°, which were indexed to the ZIF-8 (0 1 1), (0 0 2), (1 1 2), (0 2 2), (0 1 3) and (2 2 2) plane reflections. The diffraction patterns of MB-GOx-ZIF-8 and MB-GOx-ZIF-8/Au-rGO were consistent with that of ZIF-8, which demonstrates that the encapsulation of MB, GOx and the combination with Au-rGO had negligible effects on the structure of ZIF-8 hosts. The characteristic peak in MB-GOx-ZIF-8/Au-rGO at 44.31° was indexed to the Au (1 1 1) plane reflection. The digital images showed the color of these nanomaterials (Fig. S2). The ZIF-8 powder was white (Fig. S2A) and the color of MB-GOx-ZIF-8 became lilac (Fig. S2B), which indicated that the MB molecules were successfully loaded into the ZIF-8. The color of Au-rGO was black (Fig. S2D). After the combination of MB-GOx-ZIF-8 and Au-rGO, the color of MB-GOx-ZIF-8/Au-rGO turned to blue grey (Fig. S2C). The Fourier transform infrared (FTIR) spectra of Au-rGO, MB, GOx, ZIF-8 and MB-GOx-ZIF-8/Au-rGO were presented in Fig. 1H. In the spectrum of Au-rGO, the adsorption peak at 3437 cm^{-1} was derived from O-H stretching vibration, corresponding to hydroxyl groups and carboxylic functional groups. The bands at 1716, 1400, and 1083 cm^{-1} corresponded to the C–O stretching vibration, the C–O–H deformation vibration, and the C=O stretching vibration, respectively. Compared to the spectrum of ZIF-8, the MB-GOx-ZIF-8/Au-rGO displayed adsorption peaks at 1640–1660 cm^{-1}, mainly attributed to C=O stretching in structure of GOx, suggesting the presence of GOx in MB-GOx-ZIF-8/Au-rGO composites. The adsorption at 1051 cm^{-1} attributed to stretching vibration of C—S bonds, which also shown in the spectrum of MB, indicating the successful encapsulation of MB molecules. Then, the enzymatic activity

of the GOx encapsulated in MB-GOx-ZIF-8/Au-rGO composites was detected by o-dianisidine indicator system shown in Fig. 1I. The detection method was shown in Supplementary material (Section S2). Horseradish peroxidase (HRP) and o-dianisidine were combined to prepare the reaction solution. After the solution containing glucose or MB-GOx-ZIF-8/Au-rGO alone added into reaction solution, the color of the mixture did not change. The addition of solution containing glucose and MB-ZIF-8/Au-rGO also did not introduce color change. Upon the addition of the mixture of glucose and MB-GOx-ZIF-8/Au-rGO, the color of the reaction solution turned orange with a characteristic absorbance peak at 440 nm, suggesting that H_2O_2 was produced in this MB-GOx-ZIF-8/Au-rGO-catalyzed reaction.

3.3. Characterization of functionalized PABA/Au-rGO

Surface charges of PABA and Au-rGO were analyzed using electrophoretic light scattering technique (Fig. S1). Zeta potentials of PABA (Fig. S1C) and Au-rGO (Fig. S1B) were 32.5 mV and −42.3 mV, respectively, suggesting that PABA polymer was successfully combined with Au-rGO through electrostatic binding. The morphologies of PABA polymer and PABA/Au-rGO were characterized by TEM. The prepared PABA polymer showed morphology of cross-linked nanofiber (Fig. S3A). After the combination of PABA polymer and Au-rGO nanosheets, PABA nanofibers were successfully loaded on Au-rGO nanosheets (Fig. S3B). The EDS pattern displayed the chemical compositions of PABA/Au-rGO (Fig. S3C). The elements of B, C, N, O and F were derived from PABA naofiber. C, O and Au elements were confirmed in Au-rGO nanosheets, revealing that the composites of PABA and Au-rGO were successfully obtained.

3.4. Stepwise fabrication procedures of the immunosensor

To monitor the stepwise construction processes of the sandwich immunosensor, cyclic voltammetry (CV) was performed in 0.01 M phosphate buffered solution containing 5.0 mM $[Fe(CN)_6]^{4-/3-}$ and 0.1 M KCl (pH 7.4) by scanning the potential from −0.2–0.6 V and the scan rate was 50 mV s^{-1} shown in Fig. 2A. The SWV measurements for modification processes of the immunosensor were performed in 10 mM phosphate buffered solution containing 0.1 M KCl (pH 7.4) with pulse amplitude of 25 mV and an increase potential of 4 mV shown in Fig. 2B. The PABA/Au-rGO modified electrode (curve b) displayed higher current response compared to that of bare electrode (curve a), due to the excellent electrical conductivity of polyaniline skeleton and Au-rGO. Owing to the poor electrical conductivity of PVA, the current response decreased after PVA chains were bound to PABA (curve c). Further current decrease (curve d) was observed when Ab_1 was incubated on electrode, revealing the successful immobilization of antibody. Subsequently, the signal current further decreased step by step when the electrodes immobilized with BSA (curve e) and CA 242 antigen (curve f). The reason was that poor conductive layers were formed by these biomolecules, retarding electron transfer. All the above results demonstrated successful modification of the immunosensor.

Electrochemical impedance spectroscopy (EIS) was performed in 0.01 M phosphate buffer containing 5.0 mM $[Fe(CN)_6]^{4-/3-}$ and 0.1 M KCl (pH 7.4) to characterize the modification procedure of the immunosensor by monitoring the interfacial impedance of different modification layers (Fig. 2C). The semicircle diameter of the Nyquist plots demonstrated to electron transfer impedance. Compared to the plots of bare electrode (curve a), the plots of PABA/Au-rGO modified electrode showed smaller semicircle (curve b), indicating PABA/Au-rGO improved the interfacial conductivity. The impedance increased step by step after the electrodes modified with PVA (curve c), Ab_1 (curve d), BSA (curve e), CA 242 antigen (curve f). These results were consistent with the measurements of CV and SWV plots, suggesting successful construction of proposed immunosensor. Due to the steric hindrance of Ab_2-MB-GOx-ZIF-8/Au-rGO nanoprobe and the non-conductive protein layer of Ab_2-CA 242 antigen, the interfacial impedance further increased after the Ab_2-MB-GOx-ZIF-8/Au-rGO nanoprobe was immobilized on the modified electrode (curve g). When the modified electrode was treated with glucose at pH = 7.4, the H_2O_2-induced decomposition of PVA/PABA made the impedance decreased (curve h). The tandem reaction triggered by multi-functionalized ZIFs nanoprobe successfully decreased the interfacial impedance.

3.5. Optimization of experimental parameters

To attain the optimum detection performance of the proposed immunosensor, the effects of treatment time and concentration of glucose on GOx-catalyzed reaction and incubation time of Ab_2-MB-GOx-ZIF-8/Au-rGO nanoprobe were investigated. The current responses increased with the increasing of the incubation time, which was attributed to the antigen-antibody reaction. Then current decrease happened after 50 min (Fig. S5A). This phenomenon could be caused by desorption of MB molecules from nanoprobe at incubation temperature of 37 °C. 50 min was chosen as optimal incubation time for the immunoassay. As shown in Fig. S5B, the current signal increased with the increase of glucose treatment time from 10 to 20 min. This experimental result declared that GOx-catalyzed reaction and H_2O_2-induced films decomposition reaction required induction period. The decomposition degree of PVA/PABA films increased with the induction time. The current responses gradually decreased from 30 to 50 min, since the PVA/PABA films decomposition reaction basically ended and desorption of MB molecules led to the decrease of current signal with the increase of treat

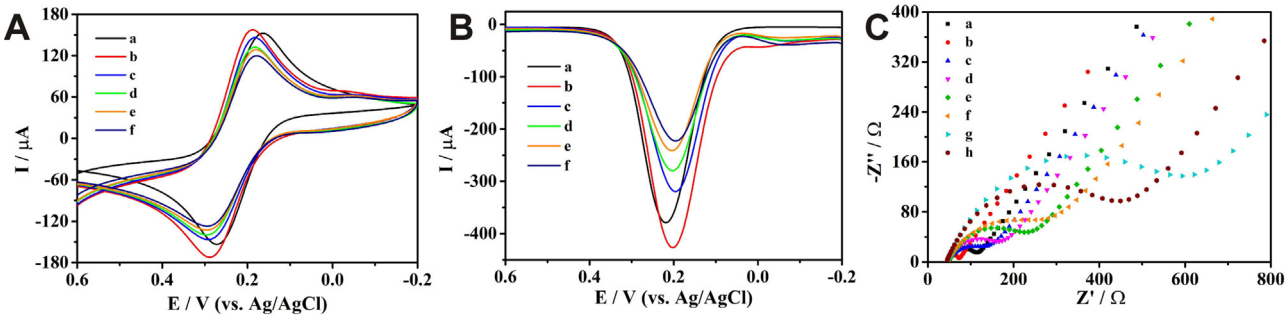

Fig. 2. CV (A) and SWV (B) of different modified electrodes in 0.01 M phosphate buffered solution containing 5.0 mM $[Fe(CN)_6]^{4-/3-}$ and 0.1 M KCl (pH 7.4): bare electrode (curve a), PABA-Au-rGO/GCE (curve b), PVA/PABA-Au-rGO/GCE (curve c), Ab_1/PVA/PABA-Au-rGO/GCE (curve d), blocked with BSA (curve e), incubated with CA 242 antigen (curve f). Nyquist plots of different modified electrodes in 0.01 M phosphate buffered solution containing 5.0 mM $[Fe(CN)_6]^{4-/3-}$ and 0.1 M KCl (pH 7.4) (C): bare electrode (curve a), PABA-Au-rGO/GCE (curve b), PVA/PABA-Au-rGO/GCE (curve c), Ab_1/PVA/PABA-Au-rGO/GCE (curve d), blocked with BSA (curve e), incubated with CA 242 antigen (curve f), incubated with functionalized ZIFs immunoprobe (curve g), treated by glucose-triggered tandem reaction (curve h).

time. 20 min was chosen as the optimum treatment time of glucose. Then, the concentration of glucose was optimized (Fig. S5C). The current responses increased with the increasing of glucose concentration from 1 to 50 mM, because the rate of PVA/PABA films decomposition reaction increased as the concentration of glucose was increased. The current response reached the plateau at 50 mM, suggesting that 50 mM was the optimum concentration of glucose.

3.6. Signal amplification of multifunctionalized ZIFs nanoprobe and tandem reaction triggered by glucose

To investigate the feasibility of the application of H_2O_2-induced decomposition reaction to the proposed immunosensing platform, the SWV measurements were performed in 0.01 M phosphate buffer containing 5.0 mM $[Fe(CN)_6]^{4-/3-}$ and 0.1 M KCl (pH 7.4) to monitor the interfacial process demonstrated in Fig. S6. The current response of PABA/Au-rGO modified electrode was up to 286.60 μA (curve a) and decreased to 153.30 μA with the modification of PVA (curve b). Then, 50 μL, 10 mM H_2O_2 in phosphate buffer at pH 7.4 was coated on the modified electrode for 30 min. After the process of H_2O_2 treatment, the modified electrode was washed with deionized water to remove the unbounded PVA chains. As shown in curve c, the current response was recovered to 260.50 μA, indicating that H_2O_2 successfully induced the decomposition of PVA/PABA on the modified electrode. To study the signal enhancement of multifunctionalized ZIFs nanprobe, Ab_2-MB/Au-rGO and Ab_2-MB-GOx-ZIF-8/Au-rGO were served as labels respectively (Fig. 3A). After the immunosensor was incubated with 1 U mL^{-1} CA 242 antigen and Ab_2-MB/Au-rGO labels respectively, the current response of SWV plot was up to 44.53 μA (curve a). The current signal of the immunosensor with Ab_2-MB-GOx-ZIF-8/Au-rGO labels was enhanced to 68.55 μA, due to the high MB loading capacity of multifunctionalized ZIFs. The signal amplification effect of tandem reaction triggered by glucose was investigated by SWV measurements (Fig. 3B). When the immunosensor without amplification procedure of tandem reaction triggered by glucose was incubated with 1 U mL^{-1} CA 242 antigen, the current response was up to 68.55 μA (curve a). When the immunosensor incubated with 1 U mL^{-1} CA 242 antigen was treated with glucose-triggered tandem reaction, the current response was amplified to 103.59 μA (curve b), revealing the glucose-triggered tandem reaction successfully elevated the current signal.

The signal amplification effect of tandem reaction on the SWV current responses was researched under the optimal experimental conditions. When the immunosensors without amplification procedure of tandem reaction triggered by glucose were incubated with and without 1 U mL^{-1} CA 242 antigen, the current responses were displayed in Fig. 3C. The current responses difference ($\Delta I = I - I_0$, where I and I_0 are current peak of the immunosensor incubated with and without 1 U mL^{-1} CA 242 antigen) reached about 31.36 μA. To confirm the effect of tandem reaction amplification, glucose-triggered tandem reaction was implemented in the modified electrodes which were incubated with and without 1 U mL^{-1} CA 242 antigens (Fig. 3D). The current response difference about SWV was increased to 55.23 μA, indicating that tandem reaction prominently enhanced ΔI caused by per unit concentration CA 242 to enhance detection performance of the immunosensor.

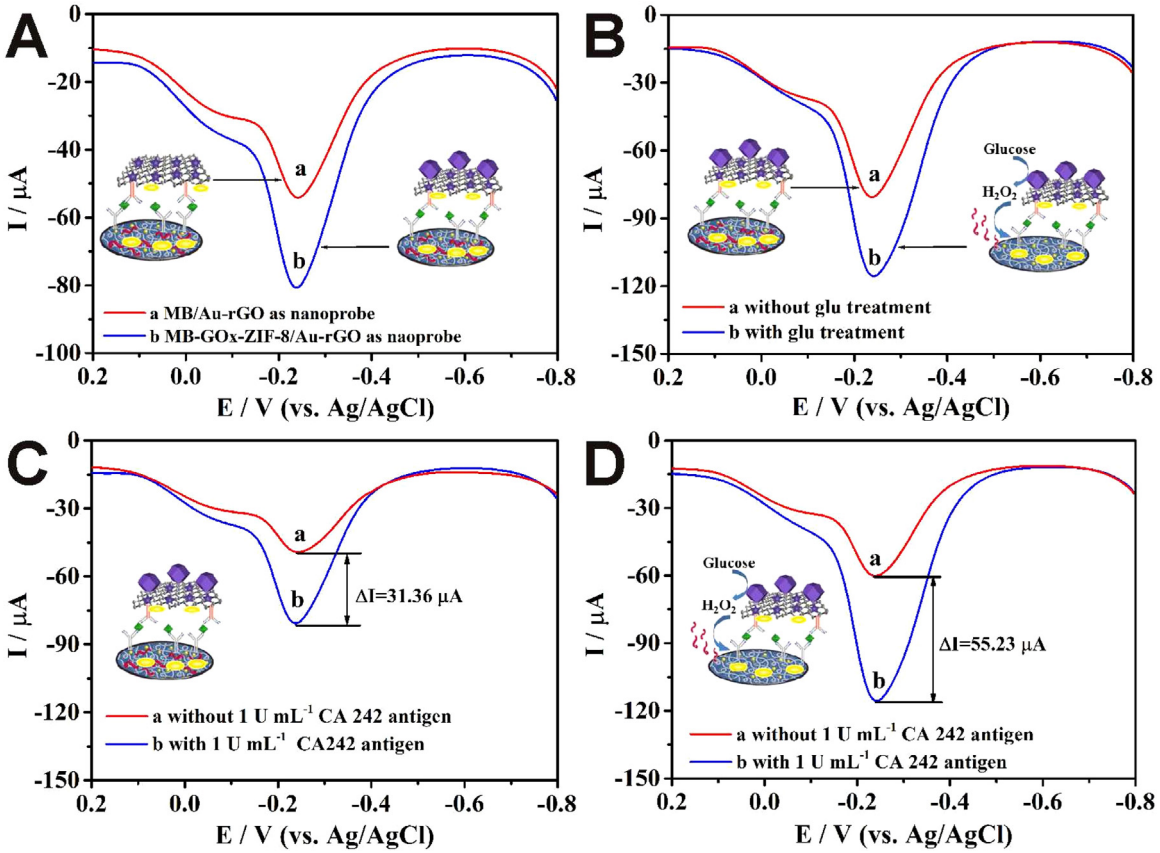

Fig. 3. SWV responses of the immunosensor with different immunoprobe (A): MB/Au-rGO as nanoprobe (curve a), MB-GOx-ZIF-8/Au-rGO as nanoprobe (curve b). SWV responses of the immunosensor incubated with 1 U mL^{-1} CA 242 (B): the immunosensor without glucose-triggered tandem reaction amplification (curve a), the immunosensor treated with glucose-triggered tandem reaction amplification (curve b). The comparisons of SWV current signal differences: the immunosensor without glucose-triggered tandem reaction amplification (C) and the immunosensor treated with glucose-triggered tandem reaction amplification (D). The immunosensor was incubated with 1 U mL^{-1} CA 242(curve b, blue lines) and without CA 242 (curve a, red lines) (in 0.01 M phosphate buffered solution containing 0.1 M KCl, pH = 7.4). (For interpretation of the references to color in this figure legend, the reader is referred to the web version of this article.)

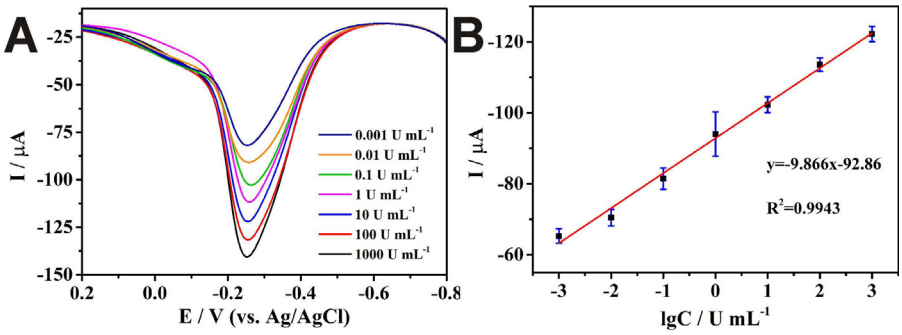

Fig. 4. (A) SWV responses of electrochemical detection for CA 242 in 0.01 M phosphate buffered solution (pH = 7.4) at the concentrations from 0.001 U mL^{-1} to 1000 U mL^{-1}. (B) The calibration plot between the SWV peak current (-0.251 V vs. Ag/AgCl) and the logarithm values of CA 242 concentrations (the error bars are standard deviations for n = 3).

3.7. Detection performance of proposed immunosensor

The SWV measurements for different concentrations of CA 242 were performed under optimal conditions. The current response increased with the elevated concentration of CA 242 ranging from 0.001 to 1000 U mL^{-1} (Fig. 4A). The calibration plot demonstrated promising relationship between the current responses and the concentrations of CA 242 antigen (Fig. 4B). The linear equation is $I = -9.866 \log_{10}C_{CA242}$-92.86, where R^2 is 0.9943. The ultrasensitive limit of detection about the immunosensor was 69.34 μU mL^{-1} at a signal-to-noise ratio of 3σ (S/N = 3) (σ is the standard deviation of signal in a black solution). Compared with the analytical assay reported in recent literatures of detection CA 199 and CA 242, the immunosensor exhibited better detection performance (Table S1).

3.8. Evaluation of specificity, repeatability and stability of the immunosensor

The specificity of the proposed immunosensor was analyzed displayed in Fig. S7A. ascorbic acid (AA), uric acid (UA), dopamine hydrochloride (DA), human serum albumin (HSA), and carcinoma antigen 125 (CA 125) were chosen as interfering substances. 1 U mL^{-1} CA 242 was mixed with AA (10 μg mL^{-1}), UA (30 μg mL^{-1}), DA (100 ng mL^{-1}), HSA (100 mg mL^{-1}), and CA 125 (100 U mL^{-1}) respectively and these solutions were incubated on the immunosensor respectively. The current responses were almost the same as that with only CA 242, showing good specificity for CA 242 of the immunosensor. The repeatability of the immunosensor was analyzed by utilizing five electrodes independently constructed with 1 U mL^{-1} CA 242 antigen. The relative standard deviation of current responses was less than 10%, indicating the acceptable repeatability (Fig. S7B). Then, the immunosensor was stored at 4 °C for four weeks and the electrochemical performance of the immunosensor for CA 242 was analyzed weekly to investigate the stability. The current response showed approximate value with the relative standard deviation of less than 10%, revealing that the stability of the immunosensor was receivable (Fig. S7C).

3.9. Determination of CA 242 in clinical serums

To evaluate the reliability of the immunosensor, CA 242 in four human serum samples were detected by the proposed immunosensor and ELISA. Every human serum sample was analyzed by immunosensor for three times. The relative errors between the results of proposed immunosensor and ELISA were less than 10% (Table S2), indicating acceptable reliability of immunosensor.

4. Conclusion

In summary, we developed a new sandwich-type immunosensor based on MB-GOx-ZIF-8/Au-rGO nanocomposite-initiated tandem reaction triggered signal amplification strategy for ultrasensitive electrochemical detection of CA 242. The multifunctionalized ZIFs nanoprobe exhibited excellent electrochemical signal and biocatalytic activity, due to its great structural features and superior conductivity. In addition, the strategy successfully combined GOx-catalyzed reaction and H_2O_2-induced film decomposition reaction in series, resulting in prominent signal amplification effect. With these advantages, the proposed immunosensor displayed wide linear range from 0.001 to 1000 U mL^{-1} with an ultralow limited of detection 69.34 μU mL^{-1} (S/N = 3) for CA 242 detection and satisfactory performance in human serum samples. However, multi-step modification process on electrode and relative long detection time limit the application of the proposed immunosensor for point-of-care diagnostics and micro-sized health monitoring devices. Therefore, facile designation of signal amplification strategy and the transfer of sandwich immune process from electrode surface to tube will be promising approaches to improve the practical application performance of sandwich-type immunosensor.

CRediT authorship contribution statement

Yun Zheng: Conceptualization, Data curation, Formal analysis, Investigation, Methodology, Writing - original draft, Writing - review & editing. **Zhanfang Ma:** Funding acquisition, Project administration, Resources, Supervision, Writing - review & editing.

Acknowledgements

This research was financed by grants from National Natural Science Foundation of China (21673143, 21273153), Natural Science Foundation of Beijing Municipality (2172016, 2132008), High-level Teachers in Beijing Municipal Universities in the Period of 13th Five-year Plan (IDHT20180517) and Capacity Building for Sci-Tech Innovation - Fundamental Scientific Research Funds (025185305000/195).

Declaration of interest statement

The authors declare no conflict of interest.

Appendix A. Supporting information

Supplementary data associated with this article can be found in the online version at doi:10.1016/j.bios.2019.01.016.

References

Hou, C., Wang, Y., Ding, Q.H., Jiang, L., Li, M., Zhu, W.W., Pan, D., Zhu, H., Liu, M.Z., 2015. Nanoscale 7, 18770–18779.
Chen, Y., Gao, S.G., Chen, J.M., Wang, G.P., Wang, Z.F., Zhou, B., Jin, C.H., Yang, Y.T., Feng, X.S., 2015. Cell Biochem. Biophys. 71, 1287–1291.
Du, D., Wang, L.M., Shao, Y.Y., Wang, J., Engelhard, M.H., Lin, Y.H., 2011. Anal. Chem. 83, 746–752.
Peng, F., Su, Y.Y., Zhong, Y.L., Fan, C.H., Lee, S.T., He, Y., 2014. Acc. Chem. Res. 47, 612–623.
Furuya, N., Kawa, S., Hasebe, O., Tokoo, M., Mukawa, K., Maejima, S., Oguchi, H., 1996. Br. J. Cancer 73, 372–376.

Hasmik, V., Hasmik, H., Qnarik, A., 2011. Clin. Biochem. 44 (S209-S209).
Hu, B., Kong, F.P., Gao, X.N., Jiang, L.L., Li, X.F., Gao, W., Xu, K.H., Tang, B., 2018. Angew. Chem. Int. Ed. 57, 5306–5309.
Iishi, H., Yamamura, H., Tatsuta, M., Okuda, S., Kitamura, T., 1986. Cancer 57, 1947–1951.
Kaushik, A., Vasudev, A., Arya, S.K., Bhansali, S., 2013. Biosens. Bioelectron. 50, 35–41.
Kreno, L.E., Leong, K., Farha, O.K., Allendorf, M., Van Duyne, R.P., Hupp, J.T., 2012. Chem. Rev. 112, 1105–1125.
Kuivila, H.G., Armour, A.G., 1957. J. Am. Chem. Soc. 79, 5659–5662.
Lai, G.S., Zheng, M., Hu, W.J., Yu, A.M., 2017. Biosens. Bioelectron. 95, 15–20.
Li, G.C., Li, Y.M., Peng, H.R., Chen, K.Z., 2011. Macromol. Rapid Commun. 32, 1195–1199.
Li, M.D., Wang, P., Li, F.Y., Chu, Q.Y., Li, Y.Y., Dong, Y.H., 2017. Biosens. Bioelectron. 87, 752–759.
Li, N., Ma, H.M., Cao, W., Wu, D., Yan, T., Du, B., Wei, Q., 2015. Biosens. Bioelectron. 74, 786–791.
Li, W.X., Shu, D., Zhang, D.S., Ma, Z.F., 2018. Sens. Actuators B 262, 50–56.
Lin, J.H., Ju, H.X., 2005. Biosens. Bioelectron. 20, 1461–1470.
Liu, S., Zhou, J., Li, H., Yin, C.Y., Lai, G.S., 2016. Electroanalysis 28, 1–8.
Lyu, F.J., Zhang, Y.F., Zare, R.N., Ge, J., Liu, Z., 2014. Nano Lett. 14, 5761–5765.
Malhotra, R., Patel, V., Vaqué, J.P., Gutkind, J.S., Rusling, J.F., 2010. Anal. Chem. 82, 3118–3123.
Pan, Y.C., Liu, Y.Y., Zeng, G.F., Zhao, L., Lai, Z.P., 2011. Chem. Commun. 47, 2071–2073.
Pujol, J.L., Cooper, E.H., Lehmann, M., Purves, D.A., Danaouta, M., Midander, J., Godard, P., Michel, F.B., 1993. Brit. J. Cancer 67, 1423–1429.
Sato, K., Takahashi, M., Ito, M., Abe, E., Anzai, J.I., 2014. Langmuir 30, 9247–9250.
Sato, K., Takahashi, M., Ito, M., Abe, E., Anzai, J.I., 2015. J. Mater. Chem. B 3, 7796–7802.
Shi, L.B., Zhu, X., Liu, T.T., Zhao, H.L., Lan, M.B., 2016. Sens. Actuators B 227, 583–590.
Su, L., Yu, W., Wei, X., Leng, X.Q., Wang, H.Z., Guo, Y.N., Huang, J.D., 2017. Biosens. Bioelectron. 88, 181–187.
Tang, Z.X., Ma, Z.F., 2017. Biosens. Bioelectron. 98, 100–112.
Tang, Z.X., Wang, L.Y., Ma, Z.F., 2016. Biosens. Bioelectron. 92, 577–582.
Villeirs, G.M., Oosterlinck, W., Vanherreweghe, E., De Meerleer, G.O., 2010. Eur. J. Radiol. 73, 352–356.
Wang, H.Q., Ma, Z.F., 2018. Sens. Actuators B 266, 46–51.
Wang, Q.Q., Zhang, X.P., Huang, L., Zhang, Z.Q., Dong, S.J., 2017. Angew. Chem. Int. Ed. 56, 16082–16085.
Wang, Z.H., Yu, G.G., Xia, J.F., Zhang, F.F., Liu, Q.Y., 2018. Microchim. Acta 185, 279–286.
Yang, H.Y., Wang, H.J., Xiong, C.Y., Chai, Y.Q., Yuan, R., 2018. Biosens. Bioelectron. 116, 16–22.
Chen, Y., Han, S., Li, X., Zhang, Z.J., Ma, S.Q., 2014. Inorg. Chem. 53, 10006–10008.
Zhang, D.S., Li, W.X., Ma, Z.F., 2018. Biosens. Bioelectron. 109, 171–176.
Zhang, S., Geryak, R., Geldmeier, J., Kim, S., Tsukruk, V.V., 2017. Chem. Rev. 117, 12942–13038.
Zhao, Y., Zheng, Y.Q., Kong, R.M., Xia, L., Qu, F.L., 2016. Biosens. Bioelectron. 75, 383–388.
Zheng, Y., Ma, Z.F., 2018. Biosens. Bioelectron. 108, 46–52.
Zhou, X.X., Guo, S.J., Gao, J.X., Zhao, J.M., Xue, S.Y., Xu, W.J., 2017. Biosens. Bioelectron. 98, 83–90.
Zhuo, Y., Gui, G.F., Chai, Y.Q., Liao, N., Xiao, K., Yuan, R., 2014. Biosens. Bioelectron. 53, 459–464.